

Iron-Catalyzed Propylene Epoxidation by Nitrous Oxide: Studies on the Effects of Alkali Metal Salts

Xiaoxing Wang, Qinghong Zhang, Sufen Yang, and Ye Wang*

State Key Laboratory of Physical Chemistry of Solid Surfaces and Department of Chemistry, College of Chemistry and Chemical Engineering, Xiamen University, Xiamen 361005, People's Republic of China

Received: August 26, 2005; In Final Form: October 23, 2005

SBA-15-supported iron catalysts with and without alkali metal salt modifications were studied for propylene oxidation by nitrous oxide. The reaction route could be dramatically changed from allylic oxidation to epoxidation by modification of the $\text{FeO}_x/\text{SBA-15}$ catalyst with alkali metal salts. The KCl-1 wt % $\text{FeO}_x/\text{SBA-15}$ (K/Fe = 5) catalyst exhibited the best catalytic performances for propylene epoxidation, over which ca. 50% propylene oxide selectivity could be gained at a 10% propylene conversion at 648 K. Characterizations with diffuse reflectance UV–Vis, XANES, and Raman spectroscopic techniques revealed that the modification with KCl increased the dispersion of the iron species and changed the local coordination of iron into a tetrahedral configuration on the inner surface of SBA-15. This tetrahedrally coordinated iron site, which was probably stabilized by potassium ions, was proposed to account for the epoxidation of propylene by nitrous oxide. At the same time, the reactivity of lattice oxygen was inhibited, and the acidity of the $\text{FeO}_x/\text{SBA-15}$ was eliminated. These changes should also contribute to the increase in the selectivity to propylene oxide. The counteranions in the alkali metal salts exerted a significant influence on the catalytic behaviors probably via an electronic effect.

Introduction

Propylene oxide (PO) is a valuable organic intermediate for the production of many useful chemicals. Currently, PO is manufactured mainly by two liquid-phase processes (i.e., the chlorhydrin and the organic hydroperoxide processes). The general disadvantages of both routes are the multiple reaction steps and the formation of coupled products in large amounts. The development of a novel process, which is both economically viable and environmentally benign, would be of great importance.

The direct epoxidation of propylene to PO with a “green” oxidant still remains one of the most challenging chemical reactions. The epoxidation of propylene in the liquid phase with H_2O_2 as an oxidant over TS-1 or with H_2 – O_2 gas mixture over Pd/TS-1 seems very promising.^{1,2} However, because of the high cost of H_2O_2 and the very low formation rate of H_2O_2 generated in situ from the H_2 – O_2 mixture, the profitability of this process is still an open question.³ Although a gas-phase heterogeneous epoxidation process is preferred because of the more convenient catalyst handling, only a few studies have succeeded in achieving high efficiency for the gas-phase epoxidation of propylene.^{4,5}

Although the gas-phase epoxidation of ethylene with O_2 over Ag/ α - Al_2O_3 has been commercialized for many years,^{6,7} the epoxidation of propylene is unsuccessful using the same catalyst.⁷ The existence of the allylic C–H bonds, which are much more active toward oxidation than the vinyl C–H bonds in ethylene, causes the lower selectivity for PO formation. The use of complex catalyst components in the presence of gas-phase promoters such as organic chloride or NO can enhance the PO formation, but PO selectivity is generally lower than

60% in the epoxidation of propylene with O_2 .⁷ Haruta and co-workers have reported that PO selectivity of more than 90% can be achieved when H_2 is co-fed with O_2 over Au–Ti-based catalysts, opening new possibilities for the gas-phase epoxidation of propylene.^{8–12}

On the other hand, N_2O has attracted much attention as an oxidant in recent years. The byproduct is only N_2 and the process using N_2O as the oxidant is thus environmentally benign. The selective oxidation of benzene to phenol with N_2O has been intensively studied over iron-containing ZSM-5.¹³ Wang and Otsuka have found that CH_4 and C_2H_6 can be oxidized to the corresponding alcohols with N_2O over an iron phosphate catalyst.¹⁴ However, the reports on the use of N_2O for epoxidation of alkenes are scarce. To our knowledge, only two other papers have reported the epoxidation of propylene with N_2O .^{15,16}

In a recent paper, we found that, when an $\text{FeO}_x/\text{SBA-15}$ catalyst was modified with alkali metal salts, the epoxidation of propylene by N_2O could proceed with high selectivities and the modifier played a crucial role in determining the reaction route.¹⁷ Alkali metal salts are known to promote many heterogeneous reactions such as ammonia synthesis and ethylene or butadiene epoxidation. In the epoxidation of ethylene by O_2 over the Ag/ α - Al_2O_3 catalyst, CsCl was the best promoter in raising the selectivity to ethylene oxide. Various roles have been proposed for CsCl, but the nature of promotion mechanism is still under debate.^{18,19} The understanding of the function of the alkali metal salts in our system will provide insights into the catalyst requirements for the occurrence of the epoxidation of propylene and the key factors in controlling the reaction route. The main objective of the present work is to elucidate the roles of the alkali metal salts in the catalysis of the iron-based heterogeneous epoxidation of propylene by N_2O via detailed characterizations.

* To whom correspondence should be addressed. E-mail: yewang@xmu.edu.cn. Fax: (+86)-592-2183047. Tel: (+86)-592-2186156.

Experimental Section

Catalyst. SBA-15, a typical mesoporous silica, was synthesized with a procedure described elsewhere.^{20,21} Typically, a homogeneous mixture composed of Pluronic P123 triblock copolymer (EO₂₀–PO₇₀–EO₂₀) as the template and tetraethyl orthosilicate (TEOS) as the source of silicon in hydrochloric acid was stirred at 313 K for 20 h and further treated at 373 K for 24 h. The resultant solid was filtered, washed, and dried in a vacuum at 313 K for 12 h. The powdery sample was finally calcined in air by heating from ambient temperature to 823 K at a rate of 1 K/min and keeping at 823 K for 6 h.

Iron was introduced into SBA-15 by an impregnation method. SBA-15 after calcination was immersed into an ethanolic solution of [Fe(acac)₃] (acac = acetylacetonate) (water content < 0.5 vol %) and was allowed to stir for 12 h at room temperature. The slurry was then dried at 343 K for ca. 4 h with continuous stirring. The powdery sample was further dried in a vacuum at 313 K for 12 h and was finally calcined in air by heating from ambient temperature to 823 K at a rate of 1 K/min and keeping at 823 K for 6 h to obtain the FeO_x/SBA-15. The alkali metal salt-modified FeO_x/SBA-15 catalysts were prepared by impregnation of the FeO_x/SBA-15 with an aqueous solution of alkali metal salt followed by drying and calcination with the same procedure described above.

Characterization. X-ray diffraction (XRD) measurements were performed with a Panalytical X'Pert Pro Super X-ray diffractometer with Cu K α radiation (40 kV, 30 mA). N₂ sorption at 77 K was carried out with a Micromeritics TriStar 3000 surface area and porosimetry analyzer to examine the porous property and the surface area for each sample. The sample was pretreated at 573 K in a vacuum for 3 h before N₂ adsorption.

Diffuse reflectance UV–Vis spectra were recorded on a Varian Cary-5000 spectrometer equipped with a diffuse-reflectance accessory. The spectra were collected at 200–800 nm with BaSO₄ as a reference. Raman spectroscopic measurements were carried out with a Renishaw UV–Vis Raman system 1000R. The UV line at 325 nm from a Kimmon IK3201R-F He–Cd laser was used as the exciting source to avoid the influence of fluorescence. A laser output of 30 mW was used, and the maximum incident power at the sample was approximate 6 mW in each measurement. As for the quantitative Raman measurements, the powdery multiwall carbon-nanotube was used as an internal standard. Each sample was mixed with the carbon-nanotube by a fixed $W_{\text{sample}}/W_{\text{carbon-nanotube}}$ ratio to give a homogeneous mixture before the measurement. The intensity of the characteristic Raman band at 1590 cm⁻¹ of carbon-nanotube was normalized to 1.0 to allow the comparison of the intensity of other Raman bands among different samples.

X-ray absorption spectroscopic measurements were carried out with synchrotron radiation at a beam line BL9A station of the Photon Factory, in the High Energy Accelerator Research Organization (Tsukuba, Japan), operated at 2.5 GeV with about 350–380 mA of ring current. All the data were recorded in X-ray fluorescence mode at room temperature using a Si(111) double crystal monochromator. Energy was calibrated with Cu K-edge absorption (8981.0 eV), and the energy resolution in the XANES region was 0.3 eV. The absorption was normalized to 1.0 at an energy position of 30 eV higher than the absorption edge. Data analyses were performed with the FACOM M1800 computer system of the Data Processing Center of Kyoto University.²²

H₂-temperature-programmed reduction (H₂-TPR) was performed using a Micromeritics AutoChem II 2920 instrument.

Typically, the sample (100 mg) was first pretreated in a quartz reactor with a gas flow containing O₂ and N₂ at 823 K for 1 h followed by purging with high-purity N₂. After the sample was cooled to 303 K, a H₂–Ar (5 vol % H₂) mixture was introduced into the reactor, and the temperature was raised to 1073 K at a rate of 10 K min⁻¹. The consumption of H₂ was monitored by a thermal conductivity detector (TCD).

NH₃-temperature-programmed desorption (NH₃-TPD) was also carried out with the Micromeritics AutoChem II 2920 equipment, which was connected with a ThermoStar GSD 301 T2 mass spectrometer (Pfeiffer Vacuum). Typically, the sample (200 mg) loaded in the quartz tube was first pretreated with an O₂–He (20 vol % O₂) gas mixture at 823 K for 30 min followed by purging with high-purity He. The adsorption of NH₃ was performed at 393 K in an NH₃–He (10 vol % NH₃) mixture for 1 h, and then the remaining or weakly adsorbed NH₃ was purged by high-purity He. TPD was performed in the He flow by raising the temperature to 873 K at a rate of 10 K min⁻¹ and then keeping at 873 K for 30 min. The desorbed NH₃ was detected by the mass spectrometer. The fragment with $m/e = 16$ was used to quantify the amount of the desorbed NH₃ because the parent peak with $m/e = 17$ was usually affected by the desorbed water.

Catalytic Reaction. The catalytic reactions were carried out using a fixed-bed reactor operated at atmospheric pressure. The catalyst was pretreated with a gas flow containing He (40 mL min⁻¹) and O₂ (10 mL min⁻¹) at 823 K for 1 h followed by purging with He (60 mL min⁻¹) at the same temperature for another 1 h. After the temperature was decreased to the desired reaction temperature, the reactant gas mixture of He, C₃H₆, and N₂O was introduced to start the reaction. The products were analyzed by two on-line gas chromatographs. All the lines and valves between the exit of the reactor and the gas chromatograph were heated to 393 K to prevent the condensation of the products. The separation of PO and other oxygenated products was achieved with a Porapak T column, and the separations of other components such as N₂, N₂O, C₃H₆, CO, and CO₂ were carried out with two other columns, Porapak Q and Molecular Sieve 5A.

Results

Catalytic Reaction. Table 1 shows the catalytic performances of the 1 wt % FeO_x/SBA-15 modified with various alkali metal or alkaline earth metal chlorides for the oxidation of C₃H₆ with N₂O. As described in our earlier paper,¹⁷ acrolein was the main product in addition to CO_x (CO and CO₂) over the FeO_x/SBA-15 without modification. The modification with the alkaline earth metal salts (CaCl₂ and BaCl₂) only caused the formation of PO with very low selectivities (<3%) although these additives were also effective for the Ag-catalyzed epoxidation of C₂H₄ or C₃H₆ by O₂.⁷ On the other hand, all the alkali metal salts worked as useful modifiers for the PO formation. The main product for the oxidation of C₃H₆ was dramatically shifted from acrolein to PO when KCl, NaCl or RbCl was used.

It is of interest to note that the presence of the alkali metal salts not only enhances the selectivity to PO but also increases the C₃H₆ conversion and the turnover frequency (TOF) under the same reaction conditions. Similar to that observed for PO selectivity, the C₃H₆ conversion and the TOF also depended strongly on the nature of the alkali metal ion. As shown in Table 1, KCl was the best modifier for the conversion of C₃H₆ to PO by N₂O. PO selectivity and yield decreased with the following sequence, KCl > NaCl > RbCl > CsCl > LiCl.

Potassium salts with various counteranions were also investigated as the modifiers. As shown in Table 2, all these

TABLE 1: Selective Oxidation of Propylene by N₂O over 1 wt % FeO_x/SBA-15 Modified with Different Alkali Metal or Alkaline Earth Metal Chloride^{a,b}

catalyst	conv. (%)	TOF ^c (h ⁻¹)	selectivity (%)				CO _x
			PO	acrolein	allyl alcohol	others ^d	
1 wt % FeO _x /SBA-15	1.2	1.9	0	42	4.5	7.5	46
LiCl-1 wt % FeO _x /SBA-15	1.3	2.1	23	12	36	6.0	23
NaCl-1 wt % FeO _x /SBA-15	3.4	5.7	66	3.4	3.3	7.3	20
KCl-1 wt % FeO _x /SBA-15	4.5	7.6	72	1.6	1.0	7.4	18
RbCl-1 wt % FeO _x /SBA-15	2.8	4.8	60	1.7	0.6	7.7	30
CsCl-1 wt % FeO _x /SBA-15	2.8	5.0	44	2.0	1.0	8.0	45
CaCl ₂ -1 wt % FeO _x /SBA-15	1.5	2.6	2.5	25	54	4.5	14
BaCl ₂ -1 wt % FeO _x /SBA-15	1.2	2.1	1.3	22	32	7.7	37

^a Reaction conditions: $P(\text{C}_3\text{H}_6) = 2.53 \text{ kPa}$, $P(\text{N}_2\text{O}) = 25.3 \text{ kPa}$; $T = 598 \text{ K}$; catalyst, 0.20 g; total flow rate, 60 mL min⁻¹. ^b For the sample with alkali metal or alkaline earth metal chloride (MCl or MCl₂), M/Fe (molar ratio) = 5/1. ^c TOF was evaluated from the moles of C₃H₆ converted per mole of Fe in the catalyst per hour. ^d Other products mainly include acetone, propionaldehyde, and acetaldehyde.

TABLE 2: Selective Oxidation of Propylene by N₂O over 1 wt % FeO_x/SBA-15 Modified with Various Potassium Salts^{a,b}

catalyst	conv. (%)	TOF ^c (h ⁻¹)	selectivity (%)				CO _x
			PO	acrolein	allyl alcohol	others ^d	
1 wt % FeO _x /SBA-15	1.2	1.9	0	42	4.5	7.5	46
KCl-1 wt % FeO _x /SBA-15	4.5	7.6	72	1.6	1.0	7.4	18
KF-1 wt % FeO _x /SBA-15	1.8	3.0	53	2.5	1.6	9.9	33
KBr-1 wt % FeO _x /SBA-15	3.8	6.6	69	1.8	1.2	11	17
KI-1 wt % FeO _x /SBA-15	1.4	2.5	35	2.7	1.3	12	49
KBH ₄ -1 wt % FeO _x /SBA-15	3.1	5.1	73	3.3	1.0	13	9.7
K ₂ CO ₃ -1 wt % FeO _x /SBA-15	1.2	2.0	40	2.8	1.2	14	42
KAc-1 wt % FeO _x /SBA-15	1.0	1.6	33	3.3	1.7	16	46
KNO ₃ -1 wt % FeO _x /SBA-15	0.2	0.32	14	16	0	14	56

^a Reaction conditions: $P(\text{C}_3\text{H}_6) = 2.53 \text{ kPa}$, $P(\text{N}_2\text{O}) = 25.3 \text{ kPa}$; $T = 598 \text{ K}$; catalyst, 0.20 g; total flow rate, 60 mL min⁻¹. ^b K/Fe (molar ratio) = 5/1. ^c TOF was evaluated from the moles of C₃H₆ converted per mole of Fe in the catalyst per hour. ^d Other products mainly include acetone, propionaldehyde and acetaldehyde.

TABLE 3: Selective Oxidation of Propylene by N₂O over FeO_x/SBA-15 and KCl-FeO_x/SBA-15^a

catalyst	conv. (%)	TOF ^b (h ⁻¹)	selectivity (%)				CO _x
			PO	acrolein	allyl alcohol	others ^c	
0.5 wt % FeO _x /SBA-15	0.7	2.3	0	57	3.7	7.3	32
KCl-0.5 wt % FeO _x /SBA-15 ^d	2.6	8.8	76	1.8	1.1	6.1	15
1 wt % FeO _x /SBA-15	1.2	1.9	0	42	4.5	7.5	46
KCl-1 wt % FeO _x /SBA-15 ^{d,e}	4.5	7.6	72	1.6	1.1	7.3	18
5 wt % FeO _x /SBA-15	1.3	0.42	0	36	2.6	7.4	54
KCl-5 wt % FeO _x /SBA-15 ^d	5.8	2.0	14	7.8	1.2	37	40
KCl-5 wt % FeO _x /SBA-15 ^e	5.0	2.0	53	3.2	1.8	17	25
10 wt % FeO _x /SBA-15	1.6	0.26	0	26	0.6	6.4	67
KCl-10 wt % FeO _x /SBA-15 ^d	5.3	0.89	3.6	6.2	1.2	35	54
KCl-10 wt % FeO _x /SBA-15 ^e	5.6	1.3	12	5.0	1.0	40	42
α-Fe ₂ O ₃	0.5	0.0080	0	10	0	5.0	85
KCl-α-Fe ₂ O ₃ ^f	trace	trace	0	0	0	0	100

^a Reaction conditions: $P(\text{C}_3\text{H}_6) = 2.5 \text{ kPa}$, $P(\text{N}_2\text{O}) = 25 \text{ kPa}$; $T = 598 \text{ K}$; catalyst, 0.2 g; total flow rate, 60 mL min⁻¹. ^b TOF was evaluated from the moles of C₃H₆ converted per mole of Fe in the catalyst per hour. ^c Other products mainly include acetone, propionaldehyde and acetaldehyde.

^d K/Si (molar ratio) = 0.04/1. ^e K/Fe (molar ratio) = 5/1. ^f K/Fe (molar ratio) = 1/1.

potassium salts could result in the occurrence of epoxidation, indicating that the K⁺ played an essential role. However, significant differences in catalytic performances were observed among these potassium salts, and still KCl was the best for PO formation.

Table 3 shows the influences of the contents of iron and/or KCl on catalytic performances of the FeO_x/SBA-15 and the KCl-FeO_x/SBA-15 catalysts. For the FeO_x/SBA-15, with an increase in iron content, the acrolein selectivity decreased remarkably and the CO_x selectivity increased sharply. For the KCl-FeO_x/SBA-15, the increase in iron content from 0.5 to 1 wt % increased the C₃H₆ conversion significantly while the PO selectivity was almost kept. However, further increases in iron content decreased the PO selectivity and the TOF remarkably even though the K/Fe ratio was varied in a large range. Therefore, it is likely that the highly dispersed iron species are

always required for either the allylic oxidation in the absence of modifiers or the epoxidation in the presence of modifiers. Further optimizations showed that the catalyst with the iron content of 1 wt % and the K/Fe molar ratio of 5 exhibited the best catalytic performances for PO formation. At 648 K, a selectivity to PO of ca. 50% could be obtained at 10% C₃H₆ conversion, while at 598 K, a PO selectivity of 86% was observed at which the C₃H₆ conversion was 1.4%.

The investigation on the effect of reaction temperature in a range of 548–648 K provided activation energy values of 69 and 75 kJ mol⁻¹ for C₃H₆ conversions over the 1 wt % FeO_x/SBA-15 and the KCl-modified 1 wt % FeO_x/SBA-15 (K/Fe = 5), respectively. This indicates that the reactions are not rate-determined by diffusion in both cases. To clarify the reaction routes over the catalysts with and without modification, we have investigated the effect of the pseudo-contact time, expressed as

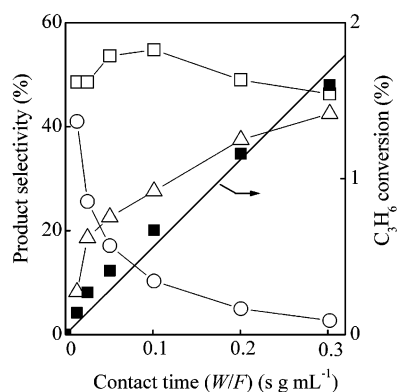


Figure 1. Changes of C_3H_6 conversion and product selectivities with contact time (W/F) over 1 wt % $FeO_x/SBA-15$ catalyst. (■) C_3H_6 conversion, selectivity to (○) allyl alcohol, (□) acrolein, (△) CO_x . Reaction conditions: $P(C_3H_6) = 2.5$ kPa, $P(N_2O) = 25$ kPa, $T = 598$ K.

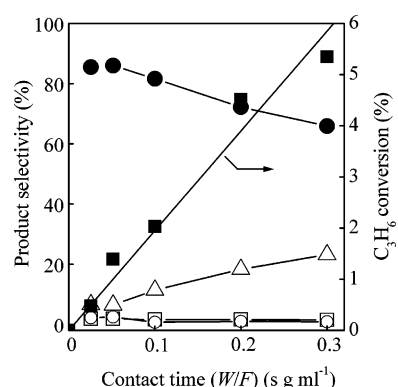


Figure 2. Changes of C_3H_6 conversion and product selectivities with contact time (W/F) over KCl-1 wt % $FeO_x/SBA-15$ ($K/Fe = 5$) catalyst. (■) C_3H_6 conversion, selectivity to (●) PO, (○) allyl alcohol, (□) acrolein, (△) CO_x . Reaction conditions: $P(C_3H_6) = 2.5$ kPa, $P(N_2O) = 25$ kPa, $T = 598$ K.

W/F , on the conversion of C_3H_6 to various products at 598 K, where W and F denote the catalyst weight and the total flow rate, respectively. The C_3H_6 conversion increased almost proportionally to the contact time over both catalysts. Figure 1 shows that the selectivity to allyl alcohol increases significantly as the contact time decreases over the 1 wt % $FeO_x/SBA-15$, suggesting that allyl alcohol is the primary product and the consecutive oxidation of allyl alcohol gives acrolein and then CO_x . On the other hand, over the KCl-modified $FeO_x/SBA-15$ catalyst, the short contact time favored the PO selectivity, and thus PO was the major primary product although the formations of minor allyl alcohol, acrolein, and CO_x were still observed at very short contact times (Figure 2). The estimated primary selectivity for PO formation was ca. 86%. The reaction pathways over the $FeO_x/SBA-15$ with and without modification by KCl are summarized in Scheme 1.

Characterizations. To uncover the effects of KCl on the catalyst structure, we have carried out detailed characterizations, mainly for the $FeO_x/SBA-15$ and the KCl-modified $FeO_x/SBA-15$.

(a) **XRD and N_2 Sorption Results.** Figure 3 shows the XRD patterns for the $FeO_x/SBA-15$ and the KCl-modified $FeO_x/SBA-15$ samples at low diffraction angles. Three diffraction lines at $2\theta^\circ$ of ca. 1.0, 1.7, and 1.9 ascribed to the hexagonal regularity of porous structure of SBA-15²⁰ were observed for all these samples, suggesting that the regularity of hexagonal arrays of mesopores of SBA-15 was sustained after the introduction of iron species and KCl.

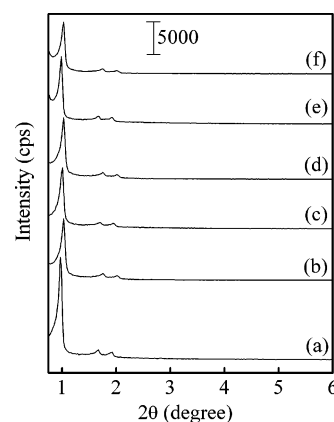


Figure 3. XRD patterns at low diffraction angles. (a) SBA-15, (b) KCl-SBA-15 ($K/Si = 0.04$), (c) 1 wt % $FeO_x/SBA-15$, (d) KCl-1 wt % $FeO_x/SBA-15$ ($K/Fe = 5$), (e) 3 wt % $FeO_x/SBA-15$, (f) KCl-3 wt % $FeO_x/SBA-15$ ($K/Fe = 5$).

SCHEME 1: Reaction Pathways for the Oxidation of C_3H_6 over the 1 wt % $FeO_x/SBA-15$ with and without Modification by KCl ($K/Fe = 5$)

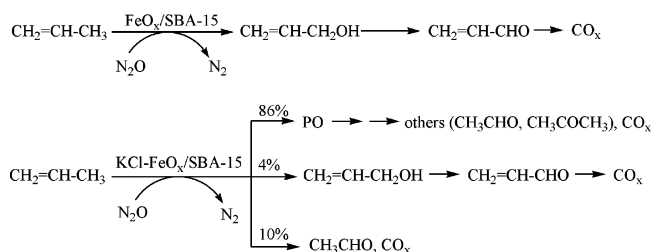


TABLE 4: Porous Properties of $FeO_x/SBA-15$ and KCl-Modified $FeO_x/SBA-15$ Determined by N_2 Sorption

sample	S_{BET} ($\text{m}^2 \text{g}^{-1}$)	pore vol ($\text{cm}^3 \text{g}^{-1}$)	mean pore diameter (nm)
SBA-15	884	1.07	6.1
1 wt % $FeO_x/SBA-15$	710	0.82	5.9
3 wt % $FeO_x/SBA-15$	671	0.82	5.7
5 wt % $FeO_x/SBA-15$	566	0.75	6.0
KCl-1 wt % $FeO_x/SBA-15$ ($K/Fe = 1$)	469	0.69	5.6
KCl-1 wt % $FeO_x/SBA-15$ ($K/Fe = 5$)	378	0.64	5.7
KCl-1 wt % $FeO_x/SBA-15$ ($K/Fe = 10$)	374	0.63	5.7
KCl-3 wt % $FeO_x/SBA-15$ ($K/Fe = 5$)	247	0.46	5.3
KCl-5 wt % $FeO_x/SBA-15$ ($K/Fe = 5$)	211	0.41	5.5

The results concerning porous properties obtained from N_2 physisorption at 77 K are shown in Table 4. Pore size distributions were determined by the BJH method (see Figure 1S for some typical samples), and all these samples exhibited narrow pore size distributions around 5.3–6.1 nm. The pore diameter for SBA-15 observed here was consistent with that reported previously.²⁰ The BET surface area and pore volume were decreased with an increase in iron content. Further decreases were observed with the addition of KCl to the $FeO_x/SBA-15$. These decreases may suggest that the mesopores of SBA-15 are filled with FeO_x and KCl species. Thus, the iron and KCl species in most of these samples are probably both located in the mesopores of SBA-15.

XRD patterns at high diffraction angles ($2\theta = 10$ – 80°) are shown in Figure 4. As the iron content was lower than 10 wt %, no diffraction peaks assigned to iron-related crystalline phases such as $\alpha\text{-Fe}_2\text{O}_3$ could be observed for the $FeO_x/SBA-15$. Peaks of $\alpha\text{-Fe}_2\text{O}_3$ were observable when the iron content reached 10 wt % (Figure 4A, curve d). For the KCl-modified 1

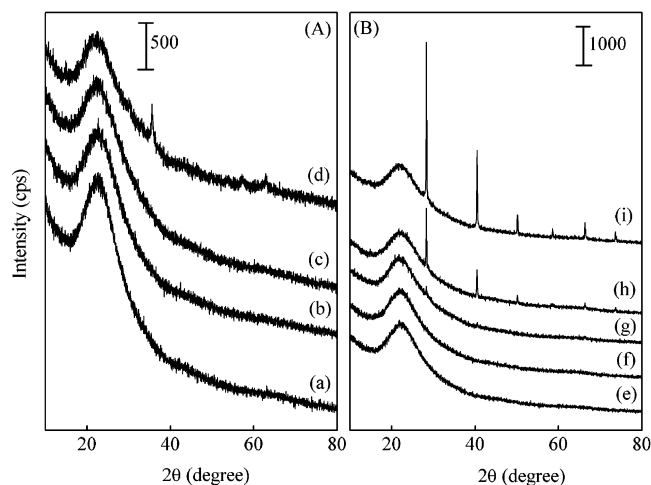


Figure 4. XRD patterns at high diffraction angles. (a) SBA-15, (b) 3 wt % $\text{FeO}_x/\text{SBA-15}$, (c) 5 wt % $\text{FeO}_x/\text{SBA-15}$, (d) 10 wt % $\text{FeO}_x/\text{SBA-15}$, (e) 1 wt % $\text{FeO}_x/\text{SBA-15}$, (f) KCl-1 wt % $\text{FeO}_x/\text{SBA-15}$ (K/Fe = 1), (g) KCl-1 wt % $\text{FeO}_x/\text{SBA-15}$ (K/Fe = 5), (h) KCl-1 wt % $\text{FeO}_x/\text{SBA-15}$ (K/Fe = 5, calcined at 673 K), (i) KCl-1 wt % $\text{FeO}_x/\text{SBA-15}$ (K/Fe = 10).

wt % $\text{FeO}_x/\text{SBA-15}$ series of samples, as the K/Fe molar ratio was lower than 5, the diffraction lines of KCl were almost unobservable (Figure 4B). The peaks of KCl became distinct for the sample with a K/Fe ratio of 10. For the KCl-1 wt % $\text{FeO}_x/\text{SBA-15}$ (K/Fe = 5; i.e., KCl, 4.7 wt %) sample, we found that the calcination temperature after the impregnation of KCl exerted significant effects on XRD patterns. As shown in Figure 4B, for the KCl-1 wt % $\text{FeO}_x/\text{SBA-15}$ (K/Fe = 5) sample calcined at a lower temperature, 673 K, the peaks of the crystalline KCl were clearly observed (curve h), whereas these peaks became almost unobservable after calcination at 823 K used normally in this work (curve g). The disappearance of the KCl crystalline phase after calcination at 823 K probably indicates a strong interaction between KCl and the iron species located in SBA-15. Such an interaction has been confirmed to be vital in obtaining high catalytic performances. The KCl-1 wt % $\text{FeO}_x/\text{SBA-15}$ (K/Fe = 5) calcined at 673 K only gave C_3H_6 conversion of 0.67% and PO selectivity of 47% under the conditions of Table 1, significantly lower than the sample calcined at 823 K (C_3H_6 conversion of 4.5% and PO selectivity of 72%).

(b) H_2 -TPR. The redox property of a catalyst is an important factor affecting its catalytic performances, particularly in selective oxidation reactions. Figure 5 shows the H_2 -TPR profiles for the $\text{FeO}_x/\text{SBA-15}$ with and without modifications. A reduction peak was observed at 682 K for the 1 wt % $\text{FeO}_x/\text{SBA-15}$ sample, and quantitative calculation revealed that this peak corresponded to the reduction of almost all the Fe^{3+} species to Fe^{2+} in this sample. The reduction peak became broader and the center shifted to a higher temperature (888–918 K, depending on the K/Fe ratio) after the modification with KCl. This result clearly indicates that the reduction of Fe^{3+} to Fe^{2+} became more difficult in the presence of KCl. The significant shift of the reduction peak for iron species after modification also indicates that there is a strong interaction existing between the iron species and KCl.

(c) NH_3 -TPD. The acid sites are detrimental to C_2H_4 epoxidation over the $\text{Ag}/\alpha\text{-Al}_2\text{O}_3$ catalyst, leading to isomerization of epoxide to acetaldehyde, followed by combustion.²³ It is recently argued convincingly that the main function of alkali metal ions over the Ag-based catalyst is the neutralization of acid sites on the oxide support.¹⁹ Here, the influence of the

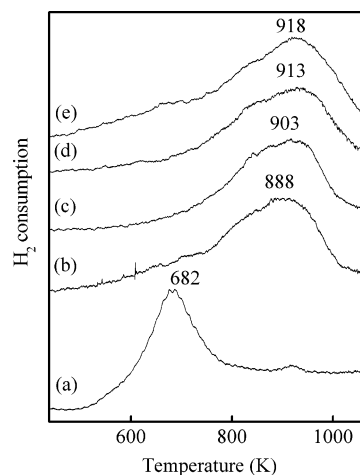


Figure 5. H_2 -TPR profiles. (a) 1 wt % $\text{FeO}_x/\text{SBA-15}$, (b) KCl-1 wt % $\text{FeO}_x/\text{SBA-15}$ (K/Fe = 2.5), (c) KCl-1 wt % $\text{FeO}_x/\text{SBA-15}$ (K/Fe = 5), (d) KCl-1 wt % $\text{FeO}_x/\text{SBA-15}$ (K/Fe = 10), (e) KCl-1 wt % $\text{FeO}_x/\text{SBA-15}$ (K/Fe = 15).

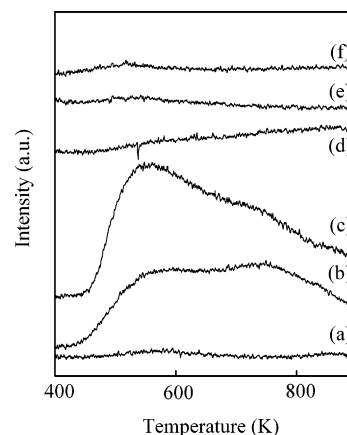


Figure 6. NH_3 -TPD profiles. (a) SBA-15, (b) 1 wt % $\text{FeO}_x/\text{SBA-15}$, (c) 5 wt % $\text{FeO}_x/\text{SBA-15}$, (d) KCl-1 wt % $\text{FeO}_x/\text{SBA-15}$ (K/Fe = 0.5), (e) KCl-1 wt % $\text{FeO}_x/\text{SBA-15}$ (K/Fe = 1), (f) KCl-1 wt % $\text{FeO}_x/\text{SBA-15}$ (K/Fe = 5).

presence of KCl on the acidity of the $\text{FeO}_x/\text{SBA-15}$ has been investigated by NH_3 -TPD measurements. NH_3 -TPD profiles obtained over the $\text{FeO}_x/\text{SBA-15}$ and the KCl-modified $\text{FeO}_x/\text{SBA-15}$ are shown in Figure 6. Almost no desorption of NH_3 has been observed over SBA-15, consistent with the fact that it does not possess acid sites. Two NH_3 desorption peaks at ca. 553 and 743 K could be observed over the $\text{FeO}_x/\text{SBA-15}$. Katada et al. studied the Fe-MFI by NH_3 -TPD and observed two NH_3 desorption peaks at ca. 550 and 723 K.²⁴ They suggested that these two peaks could be ascribed to the desorption of NH_3 adsorbed weakly on the Lewis acid sites and that strongly on the Brønsted acid sites associated with the framework iron, respectively.²⁴ Wang et al. also found two similar NH_3 -TPD peaks over the Fe-MCM-41 samples, belonging to the desorptions from the Lewis and the Brønsted acid sites.²⁵

On our occasion, although we applied impregnation method for the introduction of iron, a part of iron might interact with the Si-OH on the inner surface of SBA-15, forming disturbed -OH with relatively strong acidity. Thus, the two peaks observed over the $\text{FeO}_x/\text{SBA-15}$ could also be ascribed to the Lewis acid sites (probably the FeO_x clusters) and the Brønsted acid sites, respectively. With increasing the iron content from 1 wt % to 5 wt %, the intensity of the peak at ca. 550 K assigned to the Lewis acid sites increased significantly, while that ascribed

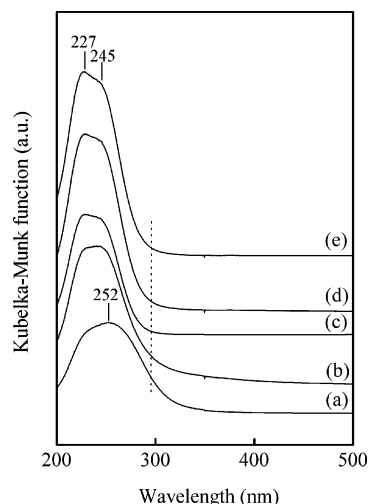


Figure 7. Diffuse reflectance UV-Vis spectra. (a) 1 wt % $\text{FeO}_x/\text{SBA-15}$, (b) KCl-1 wt % $\text{FeO}_x/\text{SBA-15}$ ($\text{K/Fe} = 0.5$), (c) KCl-1 wt % $\text{FeO}_x/\text{SBA-15}$ ($\text{K/Fe} = 1$), (d) KCl-1 wt % $\text{FeO}_x/\text{SBA-15}$ ($\text{K/Fe} = 2.5$), (e) KCl-1 wt % $\text{FeO}_x/\text{SBA-15}$ ($\text{K/Fe} = 5$).

TABLE 5: Colors and Band Gap Energy Values (Fe–O Band) for 1 wt % $\text{FeO}_x/\text{SBA-15}$ with and without Modifications as Well as $\alpha\text{-Fe}_2\text{O}_3$ and Fe–MFI

sample	color	band gap energy (eV)
$\alpha\text{-Fe}_2\text{O}_3$	rufous	2.10
Fe–MFI (Si/Fe = 100)	white	4.71
1 wt % $\text{FeO}_x/\text{SBA-15}$	pale-yellow	4.14
KCl-1 wt % $\text{FeO}_x/\text{SBA-15}$ ($\text{K/Fe} = 0.5$)	white	4.40
KCl-1 wt % $\text{FeO}_x/\text{SBA-15}$ ($\text{K/Fe} = 1$)	white	4.54
KCl-1 wt % $\text{FeO}_x/\text{SBA-15}$ ($\text{K/Fe} = 2.5$)	white	4.57
KCl-1 wt % $\text{FeO}_x/\text{SBA-15}$ ($\text{K/Fe} = 5$)	white	4.58
KCl-1 wt % $\text{FeO}_x/\text{SBA-15}$ ($\text{K/Fe} = 10$)	white	4.56

to the stronger acid sites at ca. 740 K kept almost unchanged, indicating that the iron species mainly existed on the surface as FeO_x clusters and only a limited part could interact with the Si–OH to form strong acid sites. After modification with KCl, the intensities of both peaks decreased significantly. As the ratio of K/Fe was higher than 1, almost no desorption of NH_3 could be detected. In other words, the acid sites caused by the iron species introduced into SBA-15 were eliminated by the modification with KCl, probably because of the interaction of KCl with the iron species in SBA-15.

(d) *Diffuse Reflectance UV-Visible Spectroscopy.* The color of the iron-containing sample is shown in Table 5 since it is a simple indication of whether bulk iron oxide exists.²⁶ The 1 wt % $\text{FeO}_x/\text{SBA-15}$ was pale yellow in color, possibly suggesting that it may contain small iron oxide clusters. The color changed to white after modification with KCl, indicating that the coordination structure of iron may undergo a change.

Figure 7 shows the diffuse reflectance UV-Vis spectra. The 1 wt % $\text{FeO}_x/\text{SBA-15}$ sample exhibited a broad peak at 252 nm (curve a), which could be assigned to the ligand O^{2-} to metal Fe^{3+} charge transfer (LMCT) transition. After modification with KCl, the LMCT transition shifted to shorter-wavelength positions and two peaks at 227 and 245 nm were observed. It was reported that the highly dispersed octahedral Fe^{3+} sites in Al_2O_3 showed a LMCT band at 278 nm,²⁷ while the tetrahedral Fe^{3+} sites isomorphously incorporated in the framework of MFI zeolite provided two bands at 215 and 241 nm.²⁸ For the Fe^{3+} (d^5) in the tetrahedral coordination, the high-spin $e^2t_2^3$ configuration is favored as compared with the $e^4t_2^1$ because the crystal field is not strong enough to cause spin-

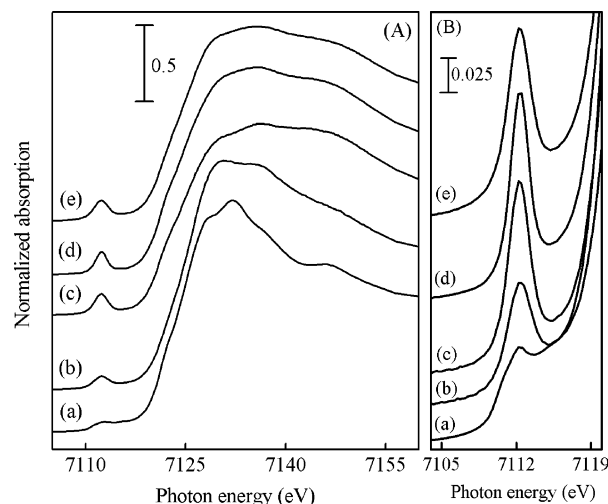


Figure 8. Fe K-edge XANES spectra (A) and preedge region (B). (a) $\alpha\text{-Fe}_2\text{O}_3$, (b) 1 wt % $\text{FeO}_x/\text{SBA-15}$, (c) KCl-1 wt % $\text{FeO}_x/\text{SBA-15}$ ($\text{K/Fe} = 0.5$), (d) KCl-1 wt % $\text{FeO}_x/\text{SBA-15}$ ($\text{K/Fe} = 5$), (e) Fe–MFI (Si/Fe = 100).

pairing. This results in the appearance of two bands assigned to $t_1 \rightarrow t_2$ and $t_1 \rightarrow e$ transitions.^{28,29} Thus, the two bands observed for the KCl– $\text{FeO}_x/\text{SBA-15}$ samples at 227 and 245 nm may suggest that Fe^{3+} ions in these samples are in tetrahedral coordination with oxygen. In other words, the modification with KCl may induce the change of iron structure from octahedral to tetrahedral configuration.

It is known that the energy of the absorption edge reflects the band gap energy of an insulator or a semiconductor and that the band gap energy is related to the domain size (dispersion) and the coordination structure of the transition metal oxides.³⁰ We have calculated the band gap energy values for the Fe–O band from the UV-Vis spectra with the method suggested by Weber³⁰ (i.e., by finding the energy intercept of the straight line in the plot of $[F(R_\infty) \times h\nu]^2$ against $h\nu$, where $F(R_\infty)$ is the Kubelka–Munk function and $h\nu$ is the incident photo energy (Figure 2S)). Two reference samples, $\alpha\text{-Fe}_2\text{O}_3$ and Fe–MFI (Si/Fe = 100), in which iron atoms are in aggregated octahedral states and isolated tetrahedral states, respectively, have also been examined. As shown in Table 5, $\alpha\text{-Fe}_2\text{O}_3$ exhibited a band gap energy value of 2.10 eV, while that for the Fe–MFI was 4.71 eV. The 1 wt % $\text{FeO}_x/\text{SBA-15}$ gave a band gap energy of 4.14 eV, which was significantly higher than that for $\alpha\text{-Fe}_2\text{O}_3$, indicating the high dispersion of small FeO_x clusters in the $\text{FeO}_x/\text{SBA-15}$. After modification with KCl, the band gap energy values increased and became close to that of the Fe–MFI. This indicates that the dispersion of iron species is further enhanced after the modification with KCl.

(e) *XANES Results.* The coordination structure of iron species has further been investigated by X-ray absorption near edge structure (XANES), which has become a reliable technique to elucidate the coordination structure of iron in molecular sieves.^{25,28,31,32} The Fe K-edge XANES spectra of the $\text{FeO}_x/\text{SBA-15}$, the KCl- and NaCl-modified $\text{FeO}_x/\text{SBA-15}$ samples are shown in Figure 8 together with the reference compounds, Fe–MFI and $\alpha\text{-Fe}_2\text{O}_3$. The two reference materials with iron in different coordination environments exhibited remarkably different XANES patterns. A clear preedge peak was observed at approximately 7112 eV for the Fe–MFI, whereas the peak was rather weaker for $\alpha\text{-Fe}_2\text{O}_3$. This preedge peak is attributed to the 1s to 3d dipolar forbidden transition. Principally, this forbidden transition gains additional intensity when the central iron atom is in a noncentral symmetric environment or through

TABLE 6: Fe K-Edge XANES Preedge Peak Areas for 1 wt % FeO_x/SBA-15 with and without Modifications as Well as Reference Compounds

sample	preedge peak area ^a	first coordination shell
4-coordinate complex ^b	23.1~25.0	O, N, S, or Cl
5-coordinate complex ^b	12.4~18.8	O, N, S, or Cl
6-coordinate complex ^b	5.8~9.3	O, N, S, or Cl
α-Fe ₂ O ₃	6.1	O
Fe-MFI (Si/Fe = 100)	25.7	O
1 wt % FeO _x /SBA-15	14.6	O
NaCl-1 wt % FeO _x /SBA-15 (Na/Fe = 5)	25.3	O
KCl-1 wt % FeO _x /SBA-15 (K/Fe = 5)	26.1	O

^a Normalized area expressed in 10⁻² eV units. ^b See ref 37.

mixing of 3d and 4p orbitals caused by the breakdown of inversion symmetry due to the structure distortion.^{33,34} Since the local symmetry around the iron is lowered from octahedral to tetrahedral coordination, the intensity of the preedge peak tends to increase (i.e., $I_{\text{octahedral}} < I_{\text{square-pyramidal}} < I_{\text{tetrahedral}}$).^{25,35,36} Therefore, the preedge peak can be used to determine the local coordination environment of iron. The absorption in Figure 8 has been normalized, and thus the intensity of the preedge peak could be compared among different samples. As shown in Figure 8B, the Fe-MFI in which iron is in a regular tetrahedral coordination showed remarkably larger intensity than α-Fe₂O₃ with iron in distorted octahedral coordination. The peak intensity of the FeO_x/SBA-15 was lower than that of the Fe-MFI but higher than that of α-Fe₂O₃, suggesting the existence of a mixture of different coordination states of iron. On the other hand, after modification of the FeO_x/SBA-15 with KCl or NaCl, the intensity of the preedge peak increased significantly.

The intensity of the preedge peak, expressed with integrated peak area, is summarized in Table 6. Roe et al. once investigated the intensity of the Fe K-edge XANES preedge peak for 28 kinds of iron complexes with different coordinations.³⁷ The areas of the preedge peaks for four-, five-, and six-coordinated iron complexes are also listed in Table 6. The peak areas for the Fe-MFI and α-Fe₂O₃ obtained in our work were approximately the same with those for the four- and six-coordinated iron complexes, respectively. The KCl-FeO_x/SBA-15 and NaCl-FeO_x/SBA-15 exhibited almost the same peak areas with those for the Fe-MFI and the four-coordinated iron complexes. Furthermore, the oscillation by XANES appearing at the high-energy region for the KCl- or NaCl-modified FeO_x/SBA-15 was very similar to that for the Fe-MFI, which was different from that for the FeO_x/SBA-15 (Figure 8A). These results strongly suggest that the local structure of iron in the KCl- or NaCl-modified FeO_x/SBA-15 is different from that in the FeO_x/SBA-15 and has changed into a tetrahedral coordination.

(f) *Raman Spectroscopy.* Figure 9 shows the Raman spectra of the FeO_x/SBA-15 and the KCl-modified FeO_x/SBA-15 samples along with SBA-15 and KCl-SBA-15 without iron. SBA-15 showed two weak Raman bands at 810 and 981 cm⁻¹, which probably originated from the asymmetrical stretching vibrations of ≡Si-OH in the defect sites of SBA-15. These two bands were also observed over the KCl-SBA-15 sample. After the introduction of iron species into SBA-15 (1 wt % FeO_x/SBA-15), two new Raman bands at ca. 1074 and 1138 cm⁻¹ appeared. Since α-Fe₂O₃ did not show any Raman bands in this region under our measuring conditions, these two bands should be related to the dispersed iron species. An iron silicalite with iron in the silicate framework was reported to exhibit Raman bands at 1025 and 1150 cm⁻¹, and these bands were proposed to be associated with the vibration modes of the O₃SiO- units

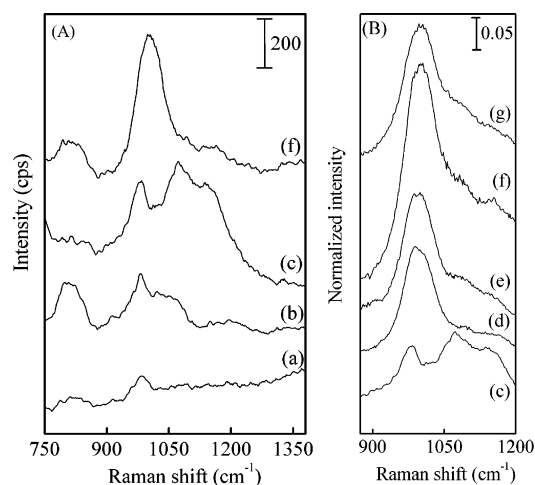


Figure 9. UV-Raman spectra. (a) SBA-15, (b) KCl-SBA-15 (K/Si = 0.04), (c) 1 wt % FeO_x/SBA-15, (d) KCl-1 wt % FeO_x/SBA-15 (K/Fe = 1), (e) KCl-1 wt % FeO_x/SBA-15 (K/Fe = 2.5), (f) KCl-1 wt % FeO_x/SBA-15 (K/Fe = 5), (g) KCl-1 wt % FeO_x/SBA-15 (K/Fe = 10).

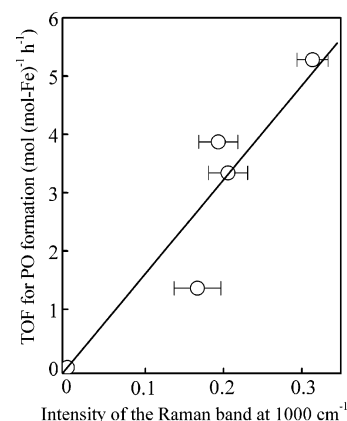


Figure 10. Turnover frequency (TOF) for PO formation vs the normalized intensity of the Raman band at 1000 cm⁻¹.

surrounding the tetrahedral Fe³⁺ center.²⁸ It was also communicated that the UV-Raman bands appearing at 1026, 1126, and 1185 cm⁻¹ were related to the contribution of the iron atoms in the framework of the ZSM-5 zeolite.³⁸ In our case, we speculate that the bands at 1074 and 1138 cm⁻¹ may be attributable to the surface iron species with strong interactions with the framework of SBA-15 as suggested by the NH₃-TPD result.

After the FeO_x/SBA-15 was modified with KCl, only one distinct band at ca. 1000 cm⁻¹ was observed in the region of 900~1200 cm⁻¹. This band could not be observed without iron and thus must stem from a novel iron structure. Combining with the UV-Vis and XANES results, we propose that this band corresponds to the tetrahedral iron sites induced by KCl on the inner surface of SBA-15. The quantitative Raman measurements with the powdery multiwall carbon-nanotube as the internal standard revealed that the intensity of the band at ca. 1000 cm⁻¹ increased with an increase in the K/Fe ratio to 5 and then decreased with a further increase in the K/Fe ratio (Figure 9B). The correlation between the formation rate (expressed as TOF) of PO and the normalized intensity of the Raman band at ca. 1000 cm⁻¹ is shown in Figure 10. The formation rate of PO increased with an increase in the intensity of the Raman band, suggesting that the KCl-induced tetrahedral iron sites giving this Raman band probably corresponded to the active species for the epoxidation of C₃H₆ by N₂O.

Discussion

As described above, we have found a very interesting shift of reaction route from allylic oxidation to epoxidation after modification of the $\text{FeO}_x/\text{SBA-15}$ with alkali metal salts typified by KCl in the oxidation of C_3H_6 by N_2O . The effects of the alkali metal salts on catalytic properties in our system are much different from those observed in C_2H_4 epoxidation by O_2 over the Ag-based catalysts. CsCl was the best promoter for C_2H_4 epoxidation, and typically, the loading amount of Cs was 200–400 ppm ($\text{Cs}/\text{Ag} = 1\sim 3 \times 10^{-3}$).^{39–41} Without the promoter, C_2H_4 could also be oxidized to ethylene oxide over the Ag/ $\alpha\text{-Al}_2\text{O}_3$. The role of the promoter was primarily limited to increasing the selectivity to ethylene oxide at the expense of C_2H_4 conversion activity. On the other hand, in our case, KCl was the best modifier and a high ratio of K/Fe ($\text{K}/\text{Fe} = 5$) was required for obtaining superior catalytic performances for PO formation. The addition of KCl dramatically changed the reaction route from allylic oxidation to epoxidation (Scheme 1). Furthermore, C_3H_6 conversion was also enhanced simultaneously. Thus, the alkali metal salts played more important roles in our case.

H_2 -TPR revealed that the reduction of Fe^{3+} to Fe^{2+} shifted significantly to higher temperatures after modification of the $\text{FeO}_x/\text{SBA-15}$ with KCl. Thus, the reactivity of the lattice oxygen associated with the iron species (FeO_x clusters) was inhibited by modification with KCl. It is well-known that the nucleophilic lattice oxygen species generally attack the allylic hydrogen and lead to allylic oxidation. Thus, the decrease in the reactivity of the lattice oxygen would suppress the allylic oxidation of propylene. This would contribute to the rise in the PO selectivity.

The modification with KCl eliminated the acidity of the $\text{FeO}_x/\text{SBA-15}$. It was reported that PO would easily isomerize to propanal and acetone under acidic circumstances, then undergo further oxidation to CO_x .⁴² Therefore, the elimination of the acid sites by KCl may decrease the probability of PO isomerization and thus may keep the high PO selectivity.

Diffuse reflectance UV–Vis, XANES and Raman spectroscopic studies revealed that the strong interaction with KCl increased the dispersion of iron species on the inner surface of SBA-15 and caused the change in the local structure of iron to a tetrahedral coordination. Generally, tetrahedrally coordinated iron can only be obtained by placing the Fe^{3+} into the framework of a zeolite or a mesoporous silica to substitute the Si^{4+} . We have thus studied the catalytic behaviors of the Fe–MFI ($\text{Si}/\text{Fe} = 100$) containing iron in the framework position for the oxidation of C_3H_6 with N_2O . Without modification with KCl, acrolein was the main product (selectivity was 46%, and C_3H_6 conversion was 1.9%) over the Fe–MFI under the reaction conditions shown in Table 1. Although PO selectivity increased from 2.0% to 33% after modification of the Fe–MFI with KCl ($\text{K}/\text{Fe} = 5$), C_3H_6 conversion decreased from 1.9% to 0.2% at the same time. The TOF for PO formation was only 0.082 h^{-1} over the KCl-modified Fe–MFI, ca. 50 times lower than that over the KCl-modified $\text{FeO}_x/\text{SBA-15}$. This strongly suggests that the iron species in the framework of MFI zeolite are less active for the epoxidation of C_3H_6 with N_2O even after the modification. We have also investigated several K- and Fe-based oxide compounds such as KFeO_2 and $\text{K}_x\text{Fe}_{22}\text{O}_{34}$,⁴³ but none of these compounds show activities in PO formation during the oxidation of C_3H_6 by N_2O . Moreover these compounds exhibited much different features in UV–Vis and Raman spectra. Therefore, the tetrahedral coordination of iron observed in our case for the KCl-modified $\text{FeO}_x/\text{SBA-15}$ should represent a new

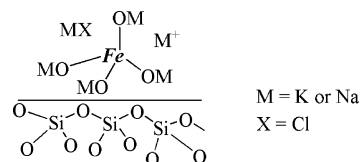


Figure 11. Possible iron site proposed for the KCl (or NaCl)-modified $\text{FeO}_x/\text{SBA-15}$.

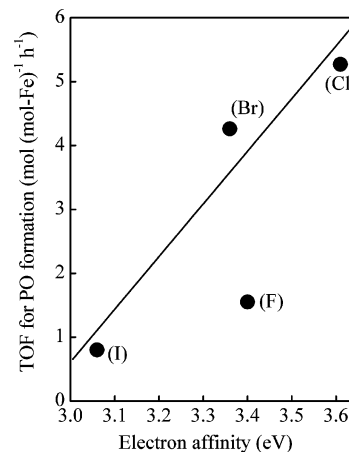


Figure 12. Turnover frequency (TOF) for PO formation vs the electronic affinity of halogen ($\text{X} = \text{F}, \text{Cl}, \text{Br}, \text{I}$).

surface structural configuration. We speculate that this tetrahedral iron site is stabilized by K^+ or Na^+ (Figure 11). The correlation between the intensity of the Raman band belonging to this iron site at ca. 1000 cm^{-1} and the TOF for PO formation suggests that this tetrahedral iron site probably accounts for the epoxidation of C_3H_6 by N_2O . We think that the formation of this new iron site is the most important role played by the KCl or NaCl. Moreover, the decrease in the reducibility of iron species and the elimination of acidity should both be the results of the change in the coordination structure of iron.

It should be recalled that, as shown in Table 2, the counteranions of potassium also exerted influences on the catalytic epoxidation of C_3H_6 by N_2O . Among the potassium salts investigated, KCl showed the best modifying effect on the formation of PO, followed by KBr and KBH_4 , whereas KAc and KNO_3 were poor modifiers. For the epoxidation of C_2H_4 by O_2 over Ag-based catalysts, Lambert et al. found that the enhancement of epoxidation selectivity correlated well with the electron affinities of the halogen modifiers.⁴⁴ By correlating the electron affinities (EA) of halogens ($\text{X} = \text{F}, \text{Cl}, \text{Br}, \text{I}$) and the catalytic performances of the KX-modified $\text{FeO}_x/\text{SBA-15}$ in Figure 12, we found that the PO formation rate increased with an increase in the EA of X except for F. The addition of KF to the $\text{FeO}_x/\text{SBA-15}$ was found to cause the collapse of the ordered mesoporous structure of SBA-15 probably due to reaction with the amorphous silica framework. This may be the reason KF is not a good modifier as expected. Therefore, we speculate that the withdrawal of the valence charge on the active oxygen by the counteranions of potassium salts may enhance its electrophilicity and thus promotes the epoxidation. The better catalytic result obtained over the KBH_4 -modified catalyst should also result from the electron-deficient nature of boron (KBH_4 was probably transferred to K_2O and B_2O_3 after calcination).

Conclusions

Highly dispersed iron species are required for the partial oxidation of propylene by N_2O . Over the $\text{FeO}_x/\text{SBA-15}$ without modification, allylic oxidation is the main reaction route,

producing acrolein and CO_x as the main products. After modification of the $\text{FeO}_x/\text{SBA-15}$ with alkali metal salts, the main reaction route shifts dramatically from allylic oxidation to epoxidation. Among a large variety of alkali metal salts, KCl exhibits the best modifying effect for PO formation. Not only PO becomes the main product, but the conversion of C_3H_6 is also enhanced after the modification.

This work has elucidated that KCl plays the following pivotal roles in accelerating the PO formation over the KCl-modified $\text{FeO}_x/\text{SBA-15}$ catalyst: (1) the reactivity of lattice oxygen associated with iron species is decreased and thus the allylic oxidation of propylene is suppressed; (2) the dispersion of iron species is further enhanced and the local coordination of iron is changed into a surface tetrahedral configuration, which probably accounts for the epoxidation of C_3H_6 by N_2O ; (3) the surface acidity derived from iron species is eliminated and thus the high PO selectivity can be kept. Among these roles, the change of the local coordination structure of iron induced by KCl is believed to be the most important. The counteranions are also crucial for obtaining higher PO formation rates probably through an electronic effect (i.e., via withdrawal of the valence change on the active oxygen to enhance its electrophilicity).

Acknowledgment. This work was supported by the NSF of China (Grants 20273054, 20021002, and 20433030), the National Basic Research Program of China (Grants 2003CB-615803 and 2005CB221408), the Program for New Century Excellent Talents in University of China (Grant NCET-04-0602), and the Scientific Research Foundation for the Returned Overseas Chinese Scholars, State Education Ministry. The authors thank Dr. T. Shishido (Tokyo Gakugai University, Japan) for the kind measurements of the X-ray absorption spectra.

Supporting Information Available: Pore size distributions for some typical samples and the plot of $[F(R_\infty)/h\nu]^2$ against $h\nu$ (Weber plot) for UV absorption edges. This material is available free of charge via the Internet at <http://pubs.acs.org>.

References and Notes

- (1) Clerici, M. G.; Bellussi, G.; Romano, U. *J. Catal.* **1991**, *129*, 159.
- (2) Meiers, R.; Dingerdissen, U.; Hölderich, W. F. *J. Catal.* **1998**, *176*, 376.
- (3) McCoy, M. *Chem. Eng. News* **2001**, *79*, 19.
- (4) Murata, K.; Kiyozumi, Y. *Chem. Commun.* **2001**, 1356.
- (5) Jewson, J. D.; Cooker, B.; Gaffney, A. M. U.S. Patent 5,780,657, 1998.
- (6) Hodnett, B. K. *Heterogeneous Catalytic Oxidation*; Wiley: Chichester, 2000.
- (7) Monnier, J. R. *Appl. Catal. A* **2001**, *221*, 73 and references therein.
- (8) Hayashi, T.; Tanaka, K.; Haruta, M. *J. Catal.* **1998**, *178*, 566.
- (9) Uphade, B. S.; Akita, T.; Nakamura, T.; Haruta, M. *J. Catal.* **2002**, *209*, 331.
- (10) Kapoor, M. P.; Sinha, A. K.; Seelan, S.; Inagaki, S.; Tsubota, S.; Yoshida, H.; Haruta, M. *Chem. Commun.* **2002**, 2902.
- (11) Sinha, A. K.; Seelan, S.; Tsubota, S.; Haruta, M. *Angew. Chem., Int. Ed.* **2004**, *43*, 1546.
- (12) Sinha, A. K.; Seelan, S.; Okumura, M.; Akita, T.; Tsubota, S.; Haruta, M. *J. Phys. Chem. B* **2005**, *109*, 3956.
- (13) Panov, G. I. *Cattech* **2000**, *4*, 18 and references therein.
- (14) Wang, Y.; Otsuka, K. *J. Chem. Soc., Faraday Trans.* **1995**, *91*, 3953.
- (15) Duma, V.; Hönicke, D. *J. Catal.* **2000**, *191*, 93.
- (16) Ananieva, E.; Reitzmann, A. *Chem. Eng. Sci.* **2004**, *59*, 5509.
- (17) Wang, X.; Zhang, Q.; Guo, Q.; Lou, Y.; Yang, L.; Wang, Y. *Chem. Commun.* **2004**, 1396.
- (18) Linic, S.; Barteau, M. A. *J. Am. Chem. Soc.* **2004**, *126*, 8086.
- (19) Williams, F. J.; Bird, D. P. C.; Palermo, A.; Santra, A. K.; Lambert, R. M. *J. Am. Chem. Soc.* **2004**, *126*, 8509.
- (20) (a) Zhao, D.; Feng, J.; Huo, Q.; Melosh, N.; Fredrickson, G. H.; Chmelka, B. F.; Stucky, G. D. *Science* **1998**, *279*, 548. (b) Zhao, D.; Huo, Q.; Feng, J.; Chmelka, B. F.; Stucky, G. D. *J. Am. Chem. Soc.* **1998**, *120*, 6024.
- (21) Yang, W.; Wang, X.; Guo, Q.; Zhang, Q.; Wang, Y. *New J. Chem.* **2003**, *27*, 1301.
- (22) Tanaka, T.; Yamashita, H.; Tsuchitani, R.; Funabiki, T.; Yoshida, S. *J. Chem. Soc., Faraday Trans. 1* **1988**, *84*, 2987.
- (23) Macleod, N.; Keel, J. M.; Lambert, R. M. *Catal. Lett.* **2003**, *86*, 51.
- (24) Katada, N.; Miyamoto, T.; Begum, H. A.; Naito, N.; Niwa, M.; Matsumoto, A.; Tsutsumi, K. *J. Phys. Chem. B* **2000**, *104*, 5511.
- (25) Wang, Y.; Zhang, Q.; Shishido, T.; Takehira, K. *J. Catal.* **2002**, *209*, 186.
- (26) Ratnasami, P.; Kumar, R. *Catal. Today* **1991**, *9*, 329.
- (27) Lehmann, G. *Z. Phys. Chem. Neue Folge* **1970**, *72*, 279.
- (28) Bordiga, S.; Buzzoni, R.; Geobaldo, F.; Lamberti, C.; Giamello, E.; Zecchina, A.; Leofanti, G.; Petrini, G.; Tozzola, G.; Vlaic, G. *J. Catal.* **1996**, *158*, 486.
- (29) Figgis, B. N. *Introduction of Ligand Fields*; Wiley: New York, 1966.
- (30) Weber, R. S. *J. Catal.* **1995**, *151*, 470.
- (31) Echchahed, B.; Moen, A.; Nicholson, D.; Bonneviot, L. *Chem. Mater.* **1997**, *9*, 1716.
- (32) Rey, F.; Sankar, G.; Maschmeyer, T.; Thomas, J. M.; Bell, R. G. *Top. Catal.* **1996**, *3*, 121.
- (33) Bordiga, S.; Coluccia, S.; Lamberti, C.; Marchese, L.; Zecchina, A.; Boscherini, F.; Buffa, F.; Genoni, F.; Leofanti, G.; Petrini, G.; Vlaic, G. *J. Phys. Chem.* **1994**, *98*, 4125.
- (34) Calas, G.; Petiau, J. *Solid State Commun.* **1983**, *48*, 625.
- (35) Choy, J.-H.; Yoon, J.-B.; Kim, D.-K.; Hwang, S.-H. *Inorg. Chem.* **1995**, *34*, 6524.
- (36) Wang, Y.; Ohishi, Y.; Shishido, T.; Zhang, Q.; Yang, W.; Guo, Q.; Wan, H.; Takehira, K. *J. Catal.* **2003**, *220*, 347.
- (37) Roe, A. L.; Schneider, D. J.; Mayer, R. J.; Pyrz, J. W.; Widow, J.; Que, L., Jr. *J. Am. Chem. Soc.* **1984**, *106*, 1676.
- (38) Li, C. *J. Catal.* **2003**, *216*, 203.
- (39) Lauritzen, A. M. U.S. Patent 4,761,394, 1988.
- (40) Lauritzen, A. M. U.S. Patent 4,833,261, 1989.
- (41) Monnier, J. R.; Stavinoha, J. L., Jr.; Minga, R. L. *J. Catal.* **2004**, *226*, 401.
- (42) Coxon, J. M.; MacLagan, R. G. A. R.; Rauk, A.; Thorpe, A. J.; Whalen, D. *J. Am. Chem. Soc.* **1997**, *119*, 4712.
- (43) Joseph, Y.; Ketteler, G.; Kuhrs, C.; Ranke, W.; Weiss, W.; Schlögl, R. *Phys. Chem. Chem. Phys.* **2001**, *3*, 4141.
- (44) Lambert, R. M.; Cropley, R. L.; Husain, A.; Tikhov, M. S. *Chem. Commun.* **2003**, 1184.